Monthly Notices
of the
ROYAL ASTRONOMICAL SOCIETY

Mon. Not. R. Astron. Soc. **406,** 2312–2324 (2010) doi:10.1111/j.1365-2966.2010.16877.x

Determining orbits for the Milky Way's dwarfs

H. Lux,[1⋆] J. I. Read[2] and G. Lake[1]

[1]*Department of Theoretical Physics, University of Zürich, Winterthurerstr. 190, CH-8057 Zürich, Switzerland*
[2]*Department of Physics & Astronomy, University of Leicester, University Road, Leicester LE1 7RH*

Accepted 2010 April 20. Received 2010 March 3; in original form 2010 January 8

ABSTRACT

We calculate orbits for the Milky Way dwarf galaxies with proper motions, and compare these to subhalo orbits in a high-resolution cosmological simulation. We use the simulation data to assess how well orbits may be recovered in the face of measurement errors, a time-varying triaxial gravitational potential and satellite–satellite interactions. For present measurement uncertainties, we recover the apocentre r_a and pericentre r_p to ∼40 per cent. With improved data from the *Gaia* satellite we should be able to recover r_a and r_p to ∼14 per cent, respectively. However, recovering the 3D positions and orbital phase of satellites over several orbits is more challenging. This owes primarily to the non-sphericity of the potential and satellite interactions during group infall. Dynamical friction, satellite mass-loss and the mass evolution of the main halo play a more minor role in the uncertainties.

We apply our technique to nine Milky Way dwarfs with observed proper motions. We show that their mean apocentre is lower than the mean of the most massive subhaloes in our cosmological simulation, but consistent with the most massive subhaloes that form before $z = 10$. This lends further support to the idea that the Milky Way's dwarfs formed before reionization.

Key words: methods: numerical – galaxies: dwarf – galaxies: kinematics and dynamics.

1 INTRODUCTION

The dwarf galaxies of the Milky Way (MW) provide a unique window on to galaxy formation on the smallest scales. Their close proximity allows us to resolve individual stars, obtaining detailed star formation histories (SFHs), mass measurements, proper motions and distances (Mateo 1998). Reliable determinations of the orbits of the dwarfs may then allow us to explore links between their environment and their formation history – e.g. the morphology–distance relation[1] (van den Bergh 1994). With accurate 3D determinations of their orbits, we may also determine if the dwarfs fell into the MW in groups (D'Onghia & Lake 2008; Li & Helmi 2008; Klimentowski et al. 2010) or suffered past interactions (Sales et al. 2007; Mateo, Olszewski & Walker 2008).

Knowing the orbital distributions of dwarfs may also shed new light on the 'missing satellites' problem (Klypin et al. 1999; Moore et al. 1999). Cosmological *N*-body simulations predict some ∼2000 bound dark matter subhaloes with peak circular velocity $v_{max} > 10\,km\,s^{-1}$ should orbit the MW within ∼600 kpc (Diemand, Kuhlen & Madau 2007a); yet the observational data favour only ∼50, even accounting for survey incompleteness effects (Simon & Geha 2007; Koposov et al. 2008). This discrepancy could be the result of exotic physics during inflation, or exotic dark matter models (e.g. Colín, Avila-Reese & Valenzuela 2000; Zentner & Bullock 2003). However, it could simply reflect how difficult it is for small dwarf galaxy haloes to collect gas and form stars while orbiting the MW (e.g. Dekel & Silk 1986; Efstathiou 1992; Barkana & Loeb 1999; Bullock, Kravtsov & Weinberg 2000; Benson et al. 2002; Kravtsov, Gnedin & Klypin 2004; Diemand, Madau & Moore 2005; Ricotti & Gnedin 2005; Gnedin & Kravtsov 2006; Moore et al. 2006; Read, Pontzen & Viel 2006; Koposov et al. 2009; Maccio' et al. 2010).

By comparing the orbits of the observed dwarfs with the orbits of subhaloes in the cosmological simulations, we can constrain formation models for the dwarfs. Former work has shown that the radial distributions of MW satellites are consistent with dwarf galaxies forming in the most massive haloes at high redshift (Moore et al. 2006). Using projected spatial distributions, this technique can also be applied to other galaxies (Chen et al. 2006; McConnachie & Irwin 2006). In this paper, we investigate what additional information can be obtained by using the full orbital distribution for the dwarfs.

The first dwarf to have its orbit estimated was the Large Magellanic Cloud (LMC), using proper motion measurements taken from photographic plate data (Jones, Klemola & Lin 1989). With the advent of the *Hubble Space Telescope*, we now have reliable proper motion measures for nearly all of the 'classical' dSph, the LMC

⋆E-mail: lux@physik.uzh.ch

[1]Note, however, that the recent discovery of three dwarf spheroidal galaxies (dSph) at large distances from Andromeda and the MW calls this into question (e.g. McConnachie et al. 2008).

Table 1. Dwarf data from the literature. From left- to right-hand side, the columns show Galactic longitude, Galactic latitude, distance to the sun, radial velocity, proper motions, V-band magnitude, the dynamical mass within 600 pc (M_{600}) and the data references.

Galaxy	l (°)	b (°)	d (kpc)	v_r (km s^{-1})	$\mu_\alpha \cos(\delta)$ (mas yr^{-1})	μ_δ (mas yr^{-1})	M_V (mag)	M_{600} (10^7 M$_\odot$)	References
UMi	105.0	+44.8	66 ± 3	-248 ± 2	-0.50 ± 0.17	0.22 ± 0.16	−8.9	$5.3^{+1.3}_{-1.3}$	1,2,12
Draco	86.4	34.7	82 ± 6	-293 ± 2	0.6 ± 0.4	1.1 ± 0.3	−8.8	$4.9^{+1.4}_{-1.3}$	1,3,12
Sextans	243.5	+42.3	86 ± 4	227 ± 3	0.26 ± 0.41	0.10 ± 0.44	−9.5	$0.9^{+0.4}_{-0.3}$	1,4,12
Sculptor	287.5	−83.2	79 ± 4	108 ± 3	0.09 ± 0.13	0.02 ± 0.13	−11.1	$2.7^{+0.4}_{-0.4}$	1,5,12
Carina	260.1	−22.2	101 ± 5	224 ± 3	0.22 ± 0.13	0.24 ± 0.11	−9.3	$3.4^{+0.7}_{-1.0}$	1,6,12
Fornax	237.1	−65.7	138 ± 8	53 ± 3	0.476 ± 0.046	-0.360 ± 0.041	−13.2	$4.3^{+2.7}_{-1.1}$	1,7,12
Sagittarius	5.6	−14.1	24 ± 2^a	140 ± 5	-2.35 ± 0.20^b	2.07 ± 0.20^b	−13.4	27^{+20}_{-27}	1,8,12
SMC	302.8	−44.3	58	175	1.16 ± 0.18	-1.17 ± 0.18	−17.2	10 ± 2	1,9,10,13
LMC	280.5	−32.9	49	324	2.03 ± 0.08	0.44 ± 0.05	−18.6	14 ± 3	1,10,11,14

[a]Note that recent work by Siegel et al. (2007) found a larger distance for Sagittarius of 28.4 ± 0.5 kpc. However, Kunder & Chaboyer (2009) favour something close to the older value (24.8 ± 0.8). Here we use the canonical value, but with larger error.
[b]These values are for $\mu_l \cos(b)$ and μ_b, respectively (see Section 3.1).
Data were taken from the following references. (1) Mateo (1998); (2) Piatek et al. (2005); (3) Scholz & Irwin (1994); (4) Walker et al. (2008); (5) Piatek et al. (2006); (6) Piatek et al. (2003, 2004); (7) Piatek et al. (2007); (8) Dinescu et al. (2005); (9) Kallivayalil et al. (2006a); (10) Koposov et al. (2009); (11) Kallivayalil et al. (2006b); (12) Strigari et al. (2007); (13) mass derived from mean of Hatzidimitriou et al. (1997), Stanimirović, Staveley-Smith & Jones (2004), Harris & Zaritsky (2006) and Evans & Howarth (2008); (14) mass derived from Kim et al. (1998), consistent with van der Marel et al. (2002).

and the Small Magellanic Cloud (SMC), and the Sagittarius dwarf galaxy (see Table 1). Orbits for these dwarfs have been derived in the literature by integrating backwards in a static potential chosen to model the MW (e.g. Piatek et al. 2002, 2003, 2005, 2006; Besla et al. 2007; Piatek et al. 2007; Besla et al. 2009). For the LMC and SMC, an interaction term (e.g. Bekki & Chiba 2005) as well as the effect of dynamical friction (e.g. Besla et al. 2007) is often included. Sagittarius is a particularly well-studied system since independent orbital constraints can be obtained from its tidally stripped stars (Ibata, Gilmore & Irwin 1994; Majewski et al. 2003, 2004; Johnston, Law & Majewski 2005; Chou et al. 2007).

In this paper, we investigate how well we can recover the orbits of the MW's dwarf galaxies in the face of a time-varying, triaxial, background potential and satellite–satellite interactions. We use the subhaloes taken from the high-resolution dark matter simulation Via Lactea I (VL1) (Diemand, Kuhlen & Madau 2007b) as a fake data set. We attempt to recover the known orbits of these subhaloes using the standard technique of integrating backwards in a fixed potential. Our fiducial model integrates orbits in a fixed spherical potential; however, we also examine the effects of a triaxial potential, mass evolution of the main halo, dynamical friction and mass-loss from the satellites. We apply both current measurement errors, and expected proper motion and distance errors for the *Gaia* mission (Perryman et al. 2001).

Having determined how well we can recover orbits with current and future data, we apply our technique to nine MW dwarfs with observed proper motions. We hunt for correlations between the dwarfs' SFHs and environment, and we compare our derived orbits with the subhaloes in the VL1 simulation to constrain solutions to the missing satellites problem.

This paper is organized as follows. In Section 2, we examine how well orbits can be recovered with current and future data. In Section 3, we apply our method to nine MW dwarf galaxies with measured radial velocities and proper motions. Finally, in Section 4 we present our conclusions.

2 TESTING THE METHOD

In this section, we use the high-resolution VL1 simulation of a MW mass galaxy (Diemand et al. 2007b) to determine how well we recover satellite orbits in the face of systematic and measurement errors.

2.1 Three quality measures

We devise three measures of quality for tracing back orbits of increasing difficultly. These are the comparison of true and recovered:

(i) last pericentre r_p and apocentre r_a;
(ii) r_p, r_a and the orbital period t backwards in time over N orbits;
(iii) 3D pericentre $\boldsymbol{r}_p$ and apocentre $\boldsymbol{r}_a$ backwards in time over N orbits.

The first of these three tells us the current orbit of the dwarf for comparison with cosmological simulations. It represents the minimum useful information we might obtain from a dwarf orbit. The second tells us *when* the dwarf encountered the MW, and how close it came. This allows us to compare orbits with SFHs. The third tells us the full 3D position of the dwarf as a function of time. This will reveal if dwarfs ever interacted via group infall or fast fly-by.

2.2 The simulation data

For our recovery tests, we use all 195 VL1 subhaloes[2] with mass $M > 10^7$ M$_\odot$ and distance to the centre of the main halo $r < 150$ kpc at redshift $z = 0$ (the z_0^{195} sample). These mass and radius cuts are chosen to mimic the observed distribution of dwarfs around the MW today (see Table 1). When comparing with the real dwarf data, we extract three different subsets of these subhaloes: the 50 most massive subhaloes today (z_0^{50}); the 50 most massive subhaloes before redshift $z = 10.59$ (z_{10}^{50}) and the 50 most massive subhaloes taking disc depletion into account [$z_{10}^{50}(r_d)$]. The first of these explores the idea that the dwarfs' luminosity is monotonically related to their current mass (e.g. Dekel & Silk 1986). The second explores the idea that the dwarfs form early before reionization (e.g. Efstathiou 1992). The third explores the effect of the MW disc (which is not

[2]We refer to subhaloes as 'satellites' interchangeably; see the data at http://www.ucolick.org/diemand/vl/

modelled in the VL1 simulation). D'Onghia et al. (2010) find that a disc with 10 per cent of the total galaxy mass can significantly alter the subhalo mass function within the central $r_d = 30$ kpc. We mimic this disc depletion effect by excluding all subhaloes with pericentres $r_p < r_d$, for a range of $r_d = 10, 15$ and 20 kpc.

2.3 The method

We take the present-day phase-space position of subhaloes in each of our samples and integrate them backwards in time to compare our derived orbits with the true VL1 orbits. We use a Leapfrog time integrator with adaptive time-stepping to adjust for the higher resolution required at pericentre (e.g. Press et al. 1992). We scale each time-step by a fraction of the instantaneous orbital time, similarly to Zemp et al. (2007). The apocentre r_a and pericentre r_p of each orbit (and therefore the period t) are then recovered by searching for a sign change in dr/dt, where r is the distance from the satellite to its host galaxy. For the VL1 data, we use a more sophisticated algorithm that only characterizes global extrema in the orbit around the main halo and ignores local extrema caused by satellite–satellite interactions or the satellite behaviour before falling into the main halo. We explicitly exclude the cosmological turn around as part of the real orbit. Note that for both the simulation as well as the recovered orbits, we determine half-periods $t_{1/2}$, i.e. the temporal distance between two orbital extrema. Hence, we only include orbits with two orbital extrema. By this criterion any satellites with long periods are excluded which are falling in for the first time. Whenever we write period instead of half-period, we mean the half-period multiplied by two.

2.4 The orbit-recovery models

We consider the following models for our orbit integration.

(i) The fiducial model (F) uses a static, spherical, NFW potential (Navarro, Frenk & White 1996). In F, we take parameters from the best fit to the VL1 main halo at redshift $z = 0$: $M_{200} = 1.77 \times 10^{12}\,M_\odot$, $R_{200} = 389$ kpc and $r_c = 24.6$ kpc (Diemand et al. 2007a).

(ii) The dynamical friction model (DF) uses the same potential as in model F with dynamical friction forces added (Chandrasekhar 1943). We use a radially varying Coulomb logarithm as in Hashimoto, Funato & Makino (2003). We also explore the impact of mass-loss of the infalling satellites, and the mass growth of the VL1 halo with time (see Fig. 1). We fit simple functions to the subhalo mass-loss history, and VL1 main halo mass growth with time as in Zhao (2004).

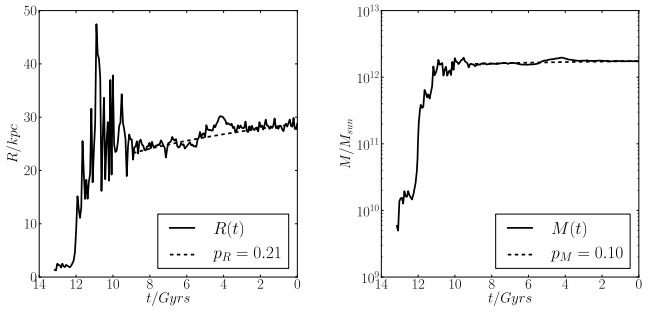

Figure 1. Evolution of the mass and scale radius of the VL1 main halo (solid line). The scale radius is more difficult to constrain for high redshifts. The dashed line is the best-fitting power law going back 9 Gyr in time.

(iii) The triaxial model (T) uses a triaxial NFW potential as in Kuhlen, Diemand & Madau (2007) and Guedes et al. (2009). We use axis ratios $q = 0.83$ and $s = 0.8$, as measured for the VL1 main halo at outer radii at $z = 0$.

(iv) The double halo mass model (2M) uses the potential as in model F, but doubling the mass of the main halo (doubling the scale radius has a negligible effect).

These different models allow us to assess the importance of systematic effects on our orbit recovery for real MW dwarf data. In practice, only model F can be realistically applied to real data since we do not know the mass-loss history of the MW dwarfs, nor the mass growth history or shape of the MW halo. We use models DF, T and 2M to explore the systematic impact of this poor knowledge on our orbit recovery.

2.5 Results

In this section, we measure how well we can recover the orbits of subhaloes in our VL1 data set. We use each of the recovery models presented in Section 2.4, with and without measurement errors and assess our results using criteria (i), (ii) and (iii) as defined in Section 2.1.

2.5.1 Perfect data

To assess the model systematics, we first consider the case without position and velocity measurement uncertainties. Figs 2–4 show our recovery for each of the models F, DF, T and 2M for the '1D' pericentres r_p and apocentres r_a, the 3D pericentres $\boldsymbol{r}_p$ and apocentres $\boldsymbol{r}_a$ and the half-period $t_{1/2}$ over N orbits. To obtain the best possible statistics, we use the z_0^{195} sample (see Section 2.2). The coloured bars show the percentage of subhaloes with fractional error $Q = 0$–0.1 (blue), 0.1–0.3 (cyan), 0.3–0.5 (green), 0.5–0.8 (red) and >0.8 (magenta). We define the relative error Q as

$$Q_p = \frac{r_p - r_{p,t}}{r_{p,t}}; \qquad Q_p(3D) = \frac{|\boldsymbol{r}_p - \boldsymbol{r}_{p,t}|}{|\boldsymbol{r}_{p,t}|} \tag{1}$$

for the '1D' pericentre (left-hand side) and 3D pericentre (right-hand side), where $r_{p,t}$ is the true pericentre and r_p is the recovered pericentre. Q is defined similarly for the other orbit quantities r_a, $\boldsymbol{r}_a$ and $t_{1/2}$. Note that in comparing r_p and $r_{p,t}$, the limited time resolution of the VL1 simulation can lead to an additional error (which causes us to always overestimate $r_{p,t}$). We tested the effect of this, finding that only orbits with $r_p \lesssim 20$ kpc are affected. The additional error due to finite time resolution is small compared to our model uncertainties.

2.5.2 Recovering the 1D pericentre and apocentre

From Fig. 2, we see that the last apocentre is well recovered in our fiducial model F. Hardly any satellites have their last apocentre recovered with greater than 30 per cent error. This is perhaps to be expected. Subhaloes are most likely to be at apocentre now and so their present position already gives a reasonable constraint on r_a. The DF and T models both improve the recovery for the most recent apocentre. This suggests that the primary reason for our error in the most recent apocentre recovery is a combination of wrong halo shape and dynamical friction, where the halo shape is more significant. By contrast, model 2M gives a poor performance, with only ∼15 per cent of the subhaloes having better than 10 per cent error on the last apocentre. This demonstrates that it is critical to

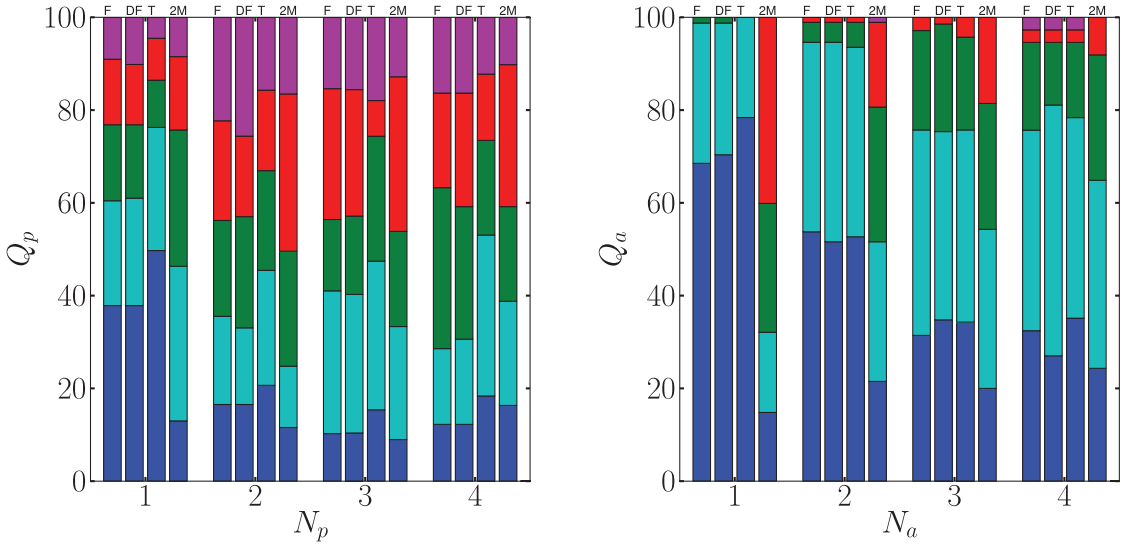

Figure 2. Orbit recovery in models F, DF, T and 2M with no measurement errors. The coloured bars show the percentage of subhaloes with fractional error $Q = 0$–0.1 (blue), 0.1–0.3 (cyan), 0.3–0.5 (green), 0.5–0.8 (red) and >0.8 (magenta) over N orbits backwards in time. In our fiducial model (F), 38 per cent of satellites have their most recent pericentres recovered to better than 10 per cent, while 69 per cent have their most recent apocentres recovered to better than 10 per cent.

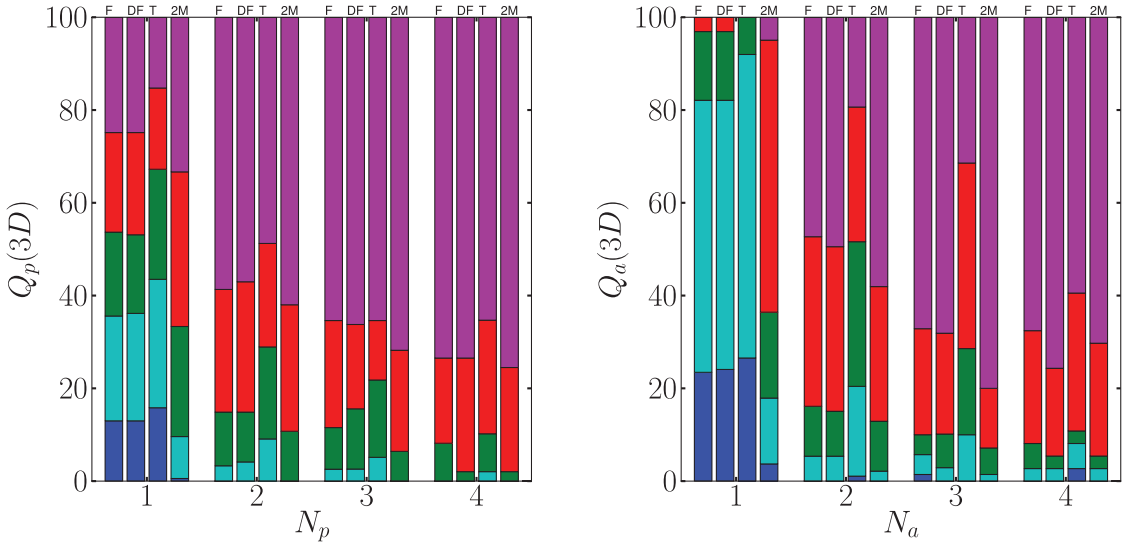

Figure 3. As Fig. 2, but for the 3D pericentre (left-hand panel) and 3D apocentre (right-hand panel).

have a good estimate of the mass of the MW interior to the orbits of its dwarfs.

The last pericentres are significantly less well recovered than the apocentres, with only 38 per cent having an error better than 10 per cent in our model F. Here the halo shape plays a major role, with model T giving a significantly better performance (∼50 per cent recovered to better than 10 per cent); dynamical friction (model DF) has little impact on the recovery. To better understand why the pericentre recovery fails, some typical example orbits from each $Q_{\rm p}$ bin are given in Fig. 5. As can be seen, orbits that have a well-recovered last $r_{\rm p}$ are *short-period* orbits. These are well recovered in model F and well recovered in the triaxial model T that has the correct current halo shape. However, long-period orbits sample the potential over several Gyr backwards in time. Here even our triaxial model (fit to the VL1 halo at redshift $z = 0$) fails and the $r_{\rm p}$ recovery is poor (see the magenta orbit).

2.5.3 Recovering orbits over several periods: the problem of group infall

Recovering orbits over several periods backwards in time is more challenging. The fraction of orbits with better than 10 per cent error in $r_{\rm a}$ in our triaxial model T drops by ∼40 per cent by $N_{\rm a} = 2$; while there are few well-recovered $r_{\rm p}$ in our model F by $N_{\rm p} = 2$. The triaxial model T gives an improvement in the recovered $r_{\rm p}$, but no improvement in $r_{\rm a}$. Note that in Fig. 2 for $N_{\rm a} = 4$ (last columns, right-hand panel) some fluctuations in the overall trends occur due to small number statistics. This happens despite our large sample z_0^{195}, as not all satellites complete four orbits within a Hubble time. Therefore individual orbits have a higher impact than they would have in a larger sample. The same is true in Fig. 3.

To understand why the errors on $r_{\rm a}$ grow so rapidly backwards in time, we give some example orbits recovered at $N_{\rm a} = 2$ in Fig. 6.

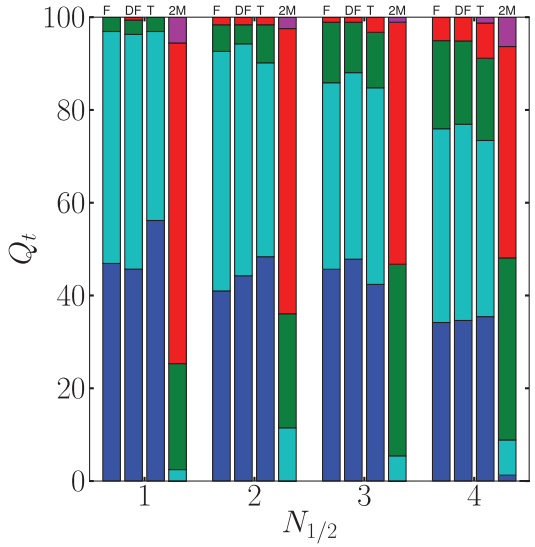

Figure 4. As Fig. 2, but for half the orbital period $t_{1/2}$.

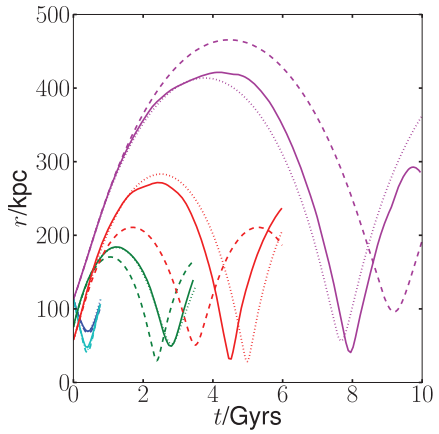

Figure 5. True and recovered orbits for the first pericentre with different Q_p values. The colours correspond to the bins in Fig. 2: $Q_p = 0$–0.1 (blue), 0.1–0.3 (cyan), 0.3–0.5 (green), 0.5–0.8 (red) and >0.8 (magenta). Solid lines are the true orbit; dashed lines are the recovered orbits in our fiducial model F and dotted lines are the recovered orbits in our triaxial model T.

As with the r_p (Fig. 5), the longer period orbits are more poorly recovered.

There is a significant class of orbits – 40 per cent – with $0.1 < Q_a < 0.3$ (cyan) that are less well recovered at $N_a = 2$. We explore a typical orbit in this class in more detail in Fig. 7. The middle panel shows our orbit recovery for the most massive subhalo in this group in models F (black dashed line), T (magenta dashed line), DF (blue dot–dashed line) and an orbit integrated with dynamical friction, but without mass-loss of the satellite or mass evolution of the main halo (green dotted line). Note that none of our models gives a good fit to the orbit. Accounting for dynamical friction and mass-loss (see right-hand panel) as well as using the triaxial potential significantly *overestimates* the apocentre. We investigated this orbit further and find this satellite to be part of a loose group. The left-hand panel shows the orbit of the satellite (black) and all subhaloes that were initially close in phase space to this satellite (red). This grouping was found by determining all satellites closer than $4r_t$, where r_t is the tidal radius defined in Diemand et al. (2007a), for at least six times outputs. These 'loose groups' usually break up at first

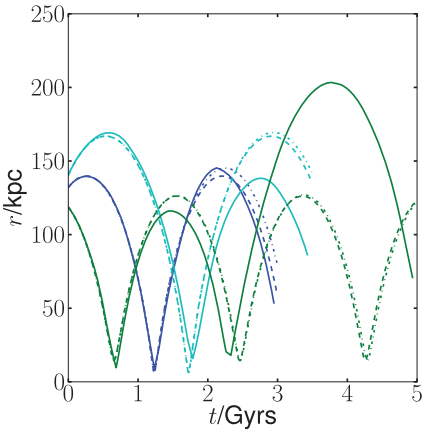

Figure 6. True and recovered orbits for the second apocentre ($N_a = 2$) with different Q_a values. The colours correspond to the bins in Fig. 2: $Q_a = 0$–0.1 (blue), 0.1–0.3 (cyan), 0.3–0.5 (green). Solid lines are the true orbit; dashed lines are the recovered orbits in our fiducial model F and dot–dashed lines are the recovered orbits in our dynamical friction model DF.

pericentre, which causes an energy change that results in lower second apocentre than we would expect from any of our integration models.

Approximately 3/4 of the satellites in the cyan bin were found to be falling into the galaxy as part of a group. This suggests that the group infall statistics recently determined by Li & Helmi (2008) may be a lower bound (see also Read et al. 2008). We defer a detailed analysis of the statistics of loose group infall to future work, but note here that it appears to be responsible for many of our poor orbit determinations at $N_a \geq 2$.

2.5.4 *Recovering the orbital phase*

In Fig. 4, we show how well we recover the half orbital period over $N_{1/2}$ orbits assuming perfect data. Note that the period is well recovered up to even two orbits backwards in time. However, in determining the *phase* of the orbit, such period errors accumulate. This makes it challenging to try and match pericentre passages with observed SFHs for the dwarfs. By $N_{1/2} = 2$, our typical phase error is 0.6 Gyr; at $N_{1/2} = 3$ it is already 0.8 Gyr. Recall that this is for *perfect data* that have no measurement errors. With current proper motion errors, recovering the orbital phase is simply not possible (see Section 2.5.6).

2.5.5 *Recovering the 3D pericentre and apocentre*

Fig. 3 shows how well we recover the 3D pericentre and apocentre for perfect data. Here having an accurate halo shape is vital. Our results in model F, even for a single orbit, are poor. Even in our triaxial model T the results, while dramatically improved, are not encouraging. This is most likely due to the radial and temporal variations in the triaxiality as found by (Kuhlen et al. 2007; Guedes et al. 2009). ∼23 per cent of the most recent 3D apocentre distances $\boldsymbol{r}_a$ and ∼13 per cent of the most recent 3D pericentre distances $\boldsymbol{r}_p$ are recovered to better than 10 per cent accuracy. Our results suggest that, unless the MW halo is close to spherical or axisymmetric, recovering full 3D orbits for the MW dwarfs will not be possible even with perfect data. This will make it difficult to determine if any of the dwarfs fell in to the MW together, or had past interactions with one another.

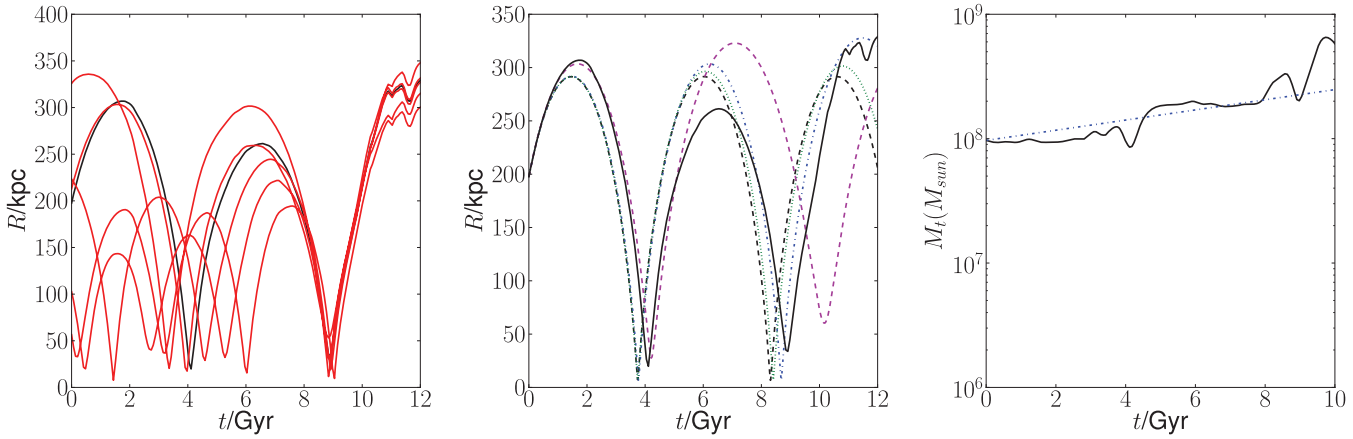

Figure 7. Group infall in the VL1 simulation. The left-hand panel shows the orbits of subhaloes that fall inside a group (red and black lines); the most massive member is shown in black. The middle panel shows our orbit recovery for the most massive subhalo in this group in models F (black dashed line), T (magenta dashed line), DF (blue dot–dashed line) and an orbit integrated with dynamical friction, but without mass-loss of the satellite or mass evolution of the main halo (green dotted line). The right-hand panel shows the mass evolution of the most massive subhalo in the group and our best-fitting curve (blue dot–dashed line) used in model DF.

2.5.6 *The effect of measurement errors*

In this section, we add the effects of measurement errors. We consider both current typical errors, and those expected in the *Gaia* era. For current errors, we use $\Delta r = 5$ kpc, $\Delta v_{\rm los} = 30$ km s^{-1} and $\Delta v_{\rm t} = 60$ km s^{-1}, where Δr is the distance error and $\Delta v_{\rm los,t}$ are the line-of-sight and tangential velocity errors, respectively (see e.g. Piatek et al. 2007). For *Gaia* errors, we use $\Delta r = 5$ kpc, $\Delta v_{\rm los} = 5$ km s^{-1} and $\Delta v_{\rm t} = 10$ km s^{-1} (see e.g. Wilkinson & Evans 1999). We determine the effects of measurement errors on our derived orbits by building an ensemble of 200 orbits drawn from the above distributions around an already defective orbit, where the defective orbit is also drawn from the same error distribution. This represents the simplest way to mimic the real measurement errors of the MW dwarfs.

We show results for our Fiducial model F in Fig. 8. We plot the true (black crosses) and recovered (blue error bars) pericentres $r_{\rm p}$, apocentres $r_{\rm a}$ and their ratio $r_{\rm p}/r_{\rm a}$. The black dashed line shows the mean of the true values, while the grey shaded band marks 1σ scatter around the mean. The blue dashed line is the mean of the recovered orbits.

For current measurement uncertainties, the error is dominated by the proper motion errors ($\Delta v_{\rm t}$). For *Gaia* errors, we are instead limited by model systematics. However, such systematics appear to average out over the whole population. Although our mean recovered $r_{\rm p}$ and $r_{\rm a}$ are both biased high by the proper motion errors, this biasing is significantly reduced with *Gaia* quality data.

2.5.7 *Orbit recovery at levels (i), (ii) and (iii)*

With current proper motion errors, we are able to recover orbits only at level (i) (the *last* pericentre $r_{\rm p}$ and apocentre $r_{\rm a}$; see Section 2.1). With *Gaia* quality data, it will be possible to recover orbits at level (ii) ($r_{\rm p}$, $r_{\rm a}$ and the orbital period t backwards in time over $N \sim 2$ orbits), though the pericentres will suffer from large systematic errors if the MW potential is triaxial. Even with perfect data, going back further than $\sim$2 orbital periods runs into the problem of group infall (see Section 2.5.3). Full 3D orbit recovery (level iii) will be extremely challenging. Recovering 3D orbit data will only be possible if the MW potential is nearly axisymmetric or spherical, and if it did not change significantly over the past $\sim$8 Gyr.

2.5.8 *Radial versus orbital distributions*

We have shown above that we can determine the *current* orbital distribution of the MW's dwarfs with available data. In Section 1, we suggested that this may provide new constraints on models that attempt to solve the missing satellites problem. In this section, we consider the advantages of using orbital distributions over simply using the *radial* distribution of the dwarfs as has been done in previous work (see e.g. Moore et al. 2006).

The mean and standard deviation of the radial distributions of our subsets z_0^{50} and z_{10}^{10} is 97 ± 32 and 87 ± 33 kpc, respectively. Former work (e.g. Kravtsov et al. 2004; Moore et al. 2006; Maccio' et al. 2010) found that the current radial distributions of the most massive satellites at $z = 0$ and the most massive satellites at high redshift ($z > 10$) differ. Further, they showed that the current radial distribution of satellites can be reproduced if they formed in the most massive haloes at high redshift. Given the mean and standard deviations of the two radial distributions of our subsets, we find it challenging to make such a distinction between the two populations. However, the values for the apocentre/pericentre distributions are much more distinct: $\langle r_{\rm a}\rangle = 237 \pm 106$, $\langle r_{\rm p}\rangle = 40 \pm 22$ for z_0^{50} and $\langle r_{\rm a}\rangle = 155 \pm 77$, $\langle r_{\rm p}\rangle = 30 \pm 15$ for z_{10}^{50}.

This surprising result can be explained by the peculiar phase distribution of the orbits in the simulation. If we take the averaged mean and standard deviation of the radial distribution over the last 2 Gyr, we find 173 ± 90 and 110 ± 60 kpc for z_0^{50} and z_{10}^{10}, respectively. On this time-scale the orbits do not change significantly, but their phases are averaged out. This shows that a comparison of the orbital distribution is necessary to reliably differentiate between different dwarf formation scenarios. (Note that previous works using the same VL1 simulation that we use here did see a difference in the radial distribution of dwarfs selected at $z = 0$ and those selected at $z = 10$. This is because they did not use the same radial and mass cuts that we employ here.)

3 APPLICATION TO THE MILKY WAY'S DWARFS

In this section, we apply our orbit-recovery technique to nine MW dwarfs with observed proper motions. With current measurement errors, we can only obtain a reliable estimate of the last pericentre

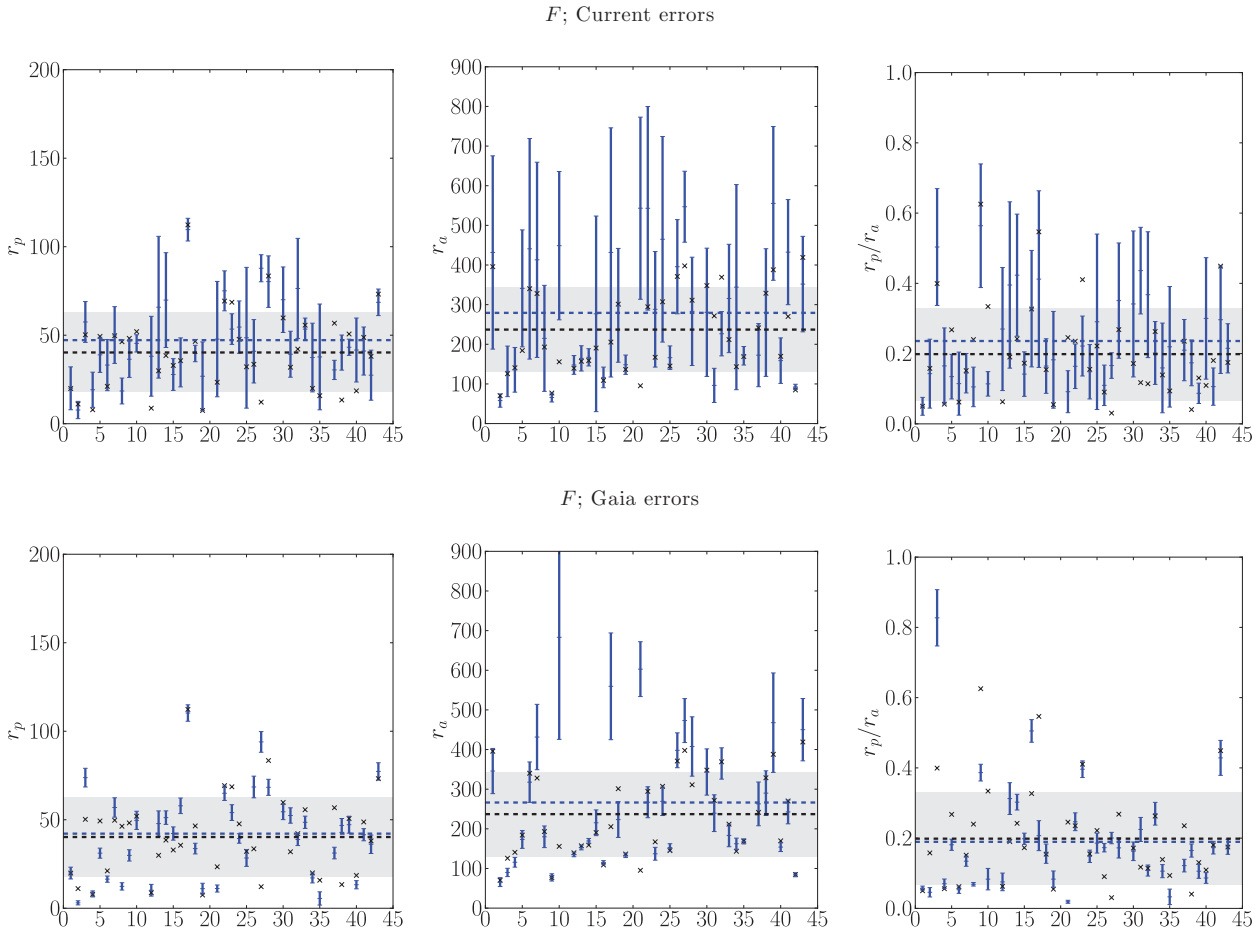

Figure 8. Orbit recovery in our Fiducial model F, with measurement errors. Panels show the pericentre, apocentre and pericentre/apocentre ratio for the 50 most massive satellites at $z = 0$ in the VL1 simulation. The black crosses correspond to the VL1 data, the blue error bars to the recovered data from the orbit integration. The black dashed horizontal lines and grey shaded area correspond to the mean and the 1σ variation of the true values, respectively. The blue dashed line corresponds to the mean of the recovered values.

and apocentre (see Section 2.5.7) and so we focus on these orbit diagnostics.

3.1 The observational data

The observational data for the nine MW dwarf galaxies with measured proper motions are summarized in Table 1. From left- to right-hand side the columns show Galactic longitude l and latitude b in degrees; the distance to the sun d in kpc; the radial velocity v_r in km s^{-1}; the proper motion data in the equatorial system $\mu_\alpha \cos(\delta)$, μ_δ in mas yr^{-1} [or in the Galactic system $\mu_l \cos(b)$, μ_b in mas yr^{-1} for Sagittarius]; the V-band magnitude M_V (mag) and the mass within 600 pc in units of 10^7 M$_\odot$. We use these as initial conditions for the orbit integration for the MW dwarfs.

We order the dwarfs by their SFH, placing them in three broad categories: those with mainly early star formation (>9 Gyr; E); those with mainly intermediate-age star formation (3–9 Gyr; I) and those with any significant recent star formation (<3 Gyr; R). Some half-categories are also introduced for galaxies that have mostly early star formation, but there is also evidence for some intermediate age (EI). The orbit data recovered in this paper as well as our classification of the SFHs and the corresponding references are summarized in Table 2.

3.2 Potentials

For the MW potential, we use two different mass models from the literature. This gives us a handle on the systematic error arising from our potential model. For our first model, we use the oblate potential from Law, Johnston & Majewski (2005) consisting of a Miyamoto–Nagai disc (Miyamoto & Nagai 1975), Hernquist spheroid (Hernquist 1990) and a logarithmic halo. The L05 model is given by

$$\Phi_{\rm disc} = -\frac{GM_{\rm disc}}{\sqrt{R^2 + \left(a + \sqrt{z^2 + b^2}\right)^2}}, \tag{2}$$

$$\Phi_{\rm sphere} = -\frac{GM_{\rm sphere}}{r + c}, \tag{3}$$

$$\Phi_{\rm halo} = v_{\rm halo}^2 \ln[R^2 + (z^2/q^2) + d^2], \tag{4}$$

with $M_{\rm disc} = 1.0 \times 10^{11}$ M$_\odot$, $a = 6.5$ kpc, b = 0.26 kpc, M$_{\rm sphere}$ = 3.4×10^{10} M$_\odot$, $c = 0.7$ kpc, v$_{\rm halo}$ = 121 km s^{-1} and $q = 0.9$.

For our second model, we use the truncated flat (TF) model from Wilkinson & Evans (1999). The TF model is given by

$$\Phi(r) = \frac{GM}{a} \log\left(\frac{\sqrt{r^2 + a^2} + a}{r}\right), \tag{5}$$

with values $M = 1.9 \times 10^{12}$ M$_\odot$ and $a = 170$ kpc.

Table 2. Derived orbits for the dwarfs, along with SFHs from the literature. From left- to right-hand side, the columns show galaxy name, pericentre in kpc, apocentre in kpc, period in Gyr, the SFH classification (see Section 3.1) and the data references. Each galaxy appears twice to show results from the L05 potential and the TF potential (see Section 3.2).

Galaxy	r_p (kpc)	r_a (kpc)	T (Gyr)	SFH	References
UMi (L05)	40 ± 20	90 ± 20	1.4 ± 0.4	E	1,2
UMi (TF)	30 ± 10	80 ± 10	1.2 ± 0.2	E	1,2
Draco (L05)	90 ± 10	300 ± 100	6 ± 2	E	1,3
Draco (TF)	74 ± 6	250 ± 80	4 ± 2	E	1,3
Sextans (L05)	70 ± 20	300 ± 200	4 ± 4	E	1,4
Sextans (TF)	60 ± 20	200 ± 100	4 ± 3	E	1,4
Sculptor (L05)	60 ± 10	160 ± 80	3 ± 1	EI	1
Sculptor (TF)	60 ± 10	130 ± 60	2 ± 1	EI	1
Carina (L05)	60 ± 30	110 ± 30	2.0 ± 0.6	I	1
Carina (TF)	50 ± 30	110 ± 30	1.8 ± 0.8	I	1
Fornax (L05)	120 ± 20	180 ± 50	4 ± 1	I	1,5
Fornax (TF)	110 ± 20	170 ± 40	4 ± 1	I	1,5
Sagittarius (L05)	12 ± 1	50 ± 7	0.7 ± 0.1	I	1
Sagittarius (TF)	12 ± 1	53 ± 5	0.56 ± 0.08	I	1
SMC (L05)	57 ± 5	200 ± 100	4 ± 1	R	1,6
SMC (TF)	56 ± 5	200 ± 100	3 ± 2	R	1,6
LMC (L05)	47 ± 1	500 ± 100	7 ± 2	R	1,7
LMC (TF)	47 ± 1	400 ± 100	7 ± 3	R	1,7

The SFH data were taken from the following references. (1) Dolphin et al. (2005); (2) Carrera et al. (2002); (3) Aparicio, Carrera & Martínez-Delgado (2001); (4) Lee et al. (2009); (5) Coleman & de Jong (2008); (6) Noël et al. (2009); (7) Harris & Zaritsky (2009).

These different models have quite different asymptotic total masses, but the mass within the orbit of the dwarfs ($\sim$150 kpc) is in reasonable accord ($\sim 6 \times 10^{11}\,M_\odot$ in the L05 model and $12 \times 10^{11}\,M_\odot$ in the TF model). The value for the VL1 is $10 \times 10^{11}\,M_\odot$ and is well within this range. We can therefore directly compare our observational results to the VL1 simulation without the need to rescale.

3.3 Model limitations and caveats

Before presenting our results for the orbital distributions of the MW dwarfs, we should discuss the limitations in our orbit-recovery method. We do not model the LMC and SMC together as is often done in the literature (e.g. Besla et al. 2007; Bekki 2008), but investigate instead their orbits independently of each other. As shown in Section 2.5.5, our model systematics are too large to determine whether or not it is better to include LMC–SMC interactions in our models, even though the existence of the Magellanic bridge certainly implies some interaction. Note that we only find bound orbits for the LMC because of the large MW masses in our models. Recent results for LMC orbits in a lower MW mass potential by Kallivayalil, van der Marel & Alcock (2006a) and Besla et al. (2007) suggest that the LMC (and with it the SMC) are falling into the MW for the first time. We find six satellites in our z_0^{50} sample that fall into the main halo for the first time. Therefore we expect roughly one out of the nine dwarfs to behave likewise. This makes a first infall scenario for the LMC not unlikely.

3.4 Results and discussion

In this section we discuss the results of our orbit integration of the nine MW dwarfs with proper motions with full evaluation of the involved errors.

3.4.1 Orbits for nine Milky Way dwarfs

In Fig. 9, we show our derived orbits for nine MW dwarf galaxies with observed proper motions. Analogous to the VL1 satellites (cf. Section 2.5.6), we estimate our errors by building an ensemble of 1000 orbits for each dwarf drawn from its error distribution. The error bars show the values for the oblate L05 potential (blue) and for the TF model (red). Overlaid are the mean and standard deviation of the values from VL1 for the 50 most massive subhaloes at $z = 0$ and for the 50 most massive subhaloes before $z = 10$, respectively (black dashed lines and grey bands). The blue dashed lines denote the mean of the VL1 subhaloes that we would recover from our orbit modelling method, assuming a typical draw from current proper motion errors (see Section 2.5.6). The difference between the blue and black dashed lines gives an estimate of the typical systematic bias introduced by our modelling method. Note that this is smaller than our quoted errors. The galaxies are ordered by their observed SFHs with those with no current star formation on the left-hand side, and those with recent star formation on the right-hand side (see Section 3.1).

The individual orbital parameters of the dwarfs given in Fig. 9 and Table 2 agree within the errors with results formerly found in the literature (Kleyna et al. 2001; Piatek et al. 2003, 2005, 2006, 2007; Walker, Mateo & Olszewski 2008). This is expected as we are using a similar set-up (initial conditions and MW mass model).

We used the smaller distance for Sagittarius in agreement with Mateo (1998) and Kunder & Chaboyer (2009), even though a higher value has been found by Siegel et al. (2007). This results in lower pericentre estimates. Law et al. (2005) find $r_p \sim 15$ kpc, $r_a \sim 60$ kpc and $t = 0.85$ Gyr as indicated by black diamonds in Fig. 9. These results differ slightly due to the different proper motions used. Even though we did not model the LMC/SMC as a pair of satellites, we still find that they are close to their pericentre now and have

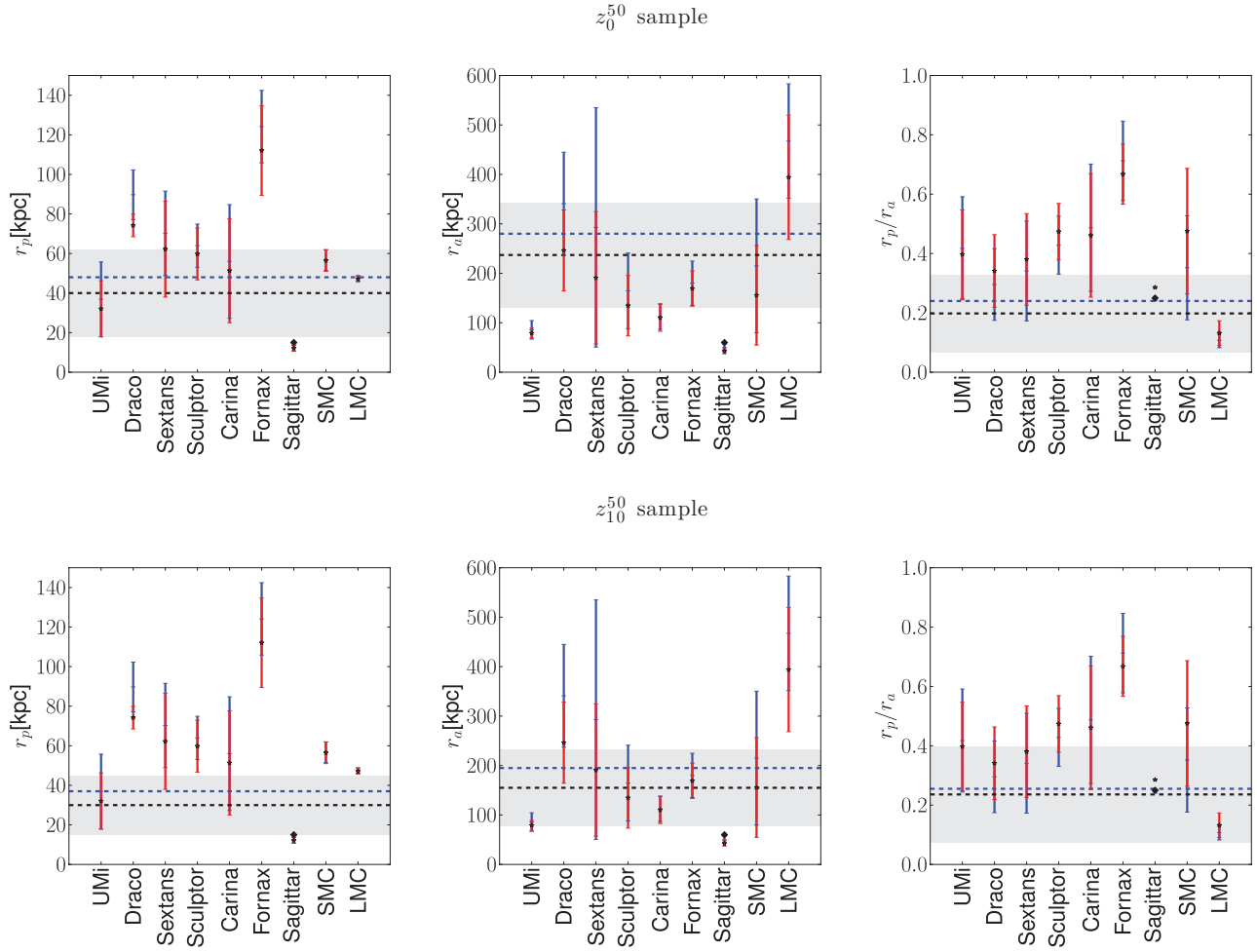

Figure 9. Recovered orbits for nine MW dwarfs with observed proper motions. The error bars show the values for the oblate L05 potential (blue) and for the TF model (red). Overlaid are the mean and standard deviation of VL1 subhaloes for the 50 most massive at $z = 0$ (z_0^{50}; top panels) and for the 50 most massive before $z = 10$ (z_{10}^{50}; bottom panels), respectively (black dashed line and grey band). We also overlay the mean for VL1 subhaloes that we would recover from our orbit modelling method, assuming a typical draw from current proper motion errors (blue dashed line; and see Section 2.5.6). The difference between the blue and black dashed lines gives an estimate of the typical systematic bias introduced by our modelling method. Note that this is smaller than our quoted errors. The galaxies are ordered by their observed SFHs with those with no current star formation on the left-hand side, and those with recent star formation on the right-hand side (see Section 3.1). The black diamonds denote the values derived from the Sagittarius stream (Law et al. 2005).

very high apocentres as has been stated before in the literature (e.g. Mastropietro et al. 2005).

3.4.2 Correlations with star formation histories

Leaving aside the three most massive satellites in our sample – Sagittarius, the SMC and the LMC – the rest of the galaxies share a similar dynamical mass (see Table 1). This makes them useful for probing how environment can promote or inhibit star formation. Blitz & Robishaw (2000), Gallart et al. (2001), Mayer et al. (2001) and Mayer & Wadsley (2004) suggest that star formation should be *enhanced* at pericentre due to tidal compression forces and increased ram pressure. However, Mayer et al. (2007) argue that the dwarf galaxies with the smallest pericentres are typically accreted early – before reionization. At these early times, the ultraviolet background radiation puffs up the gas in the dwarf making it more loosely bound and easier to tidally strip. This would lead to an overall *suppression* of star formation in dwarfs with small pericentres.

As we demonstrated in Section 2.5.7, with current proper motion errors, we cannot reliably trace the orbits of the MW's dwarfs backwards in time for more than a single orbit. Thus hunting for a correlation between observed star formation bursts and pericentre passages is not presently possible. This may explain why previous work along these lines has been inconclusive. Piatek et al. (2003, 2005, 2006, 2007) looked for correlations between the SFHs of Carina, Ursa Minor, Sculptor and Fornax and their orbits. Of all these dwarfs, only Carina shows any clear star formation bursts. But the period of Carina's orbit is too short to correlate with these bursts.

Since we cannot currently link star formation bursts to pericentre passages, we look instead for an average suppression or enhancement correlated with the dwarfs' present orbit. Fig. 9 (left-hand panel) shows our derived pericentres for the dwarfs ordered by their SFHs (see Section 3.1 and Table 2), with dwarfs that have only early star formation to the left-hand side of the plot and those with recent star formation to the right-hand side. Note that there is a very tentative tendency for dwarfs with only early star formation to

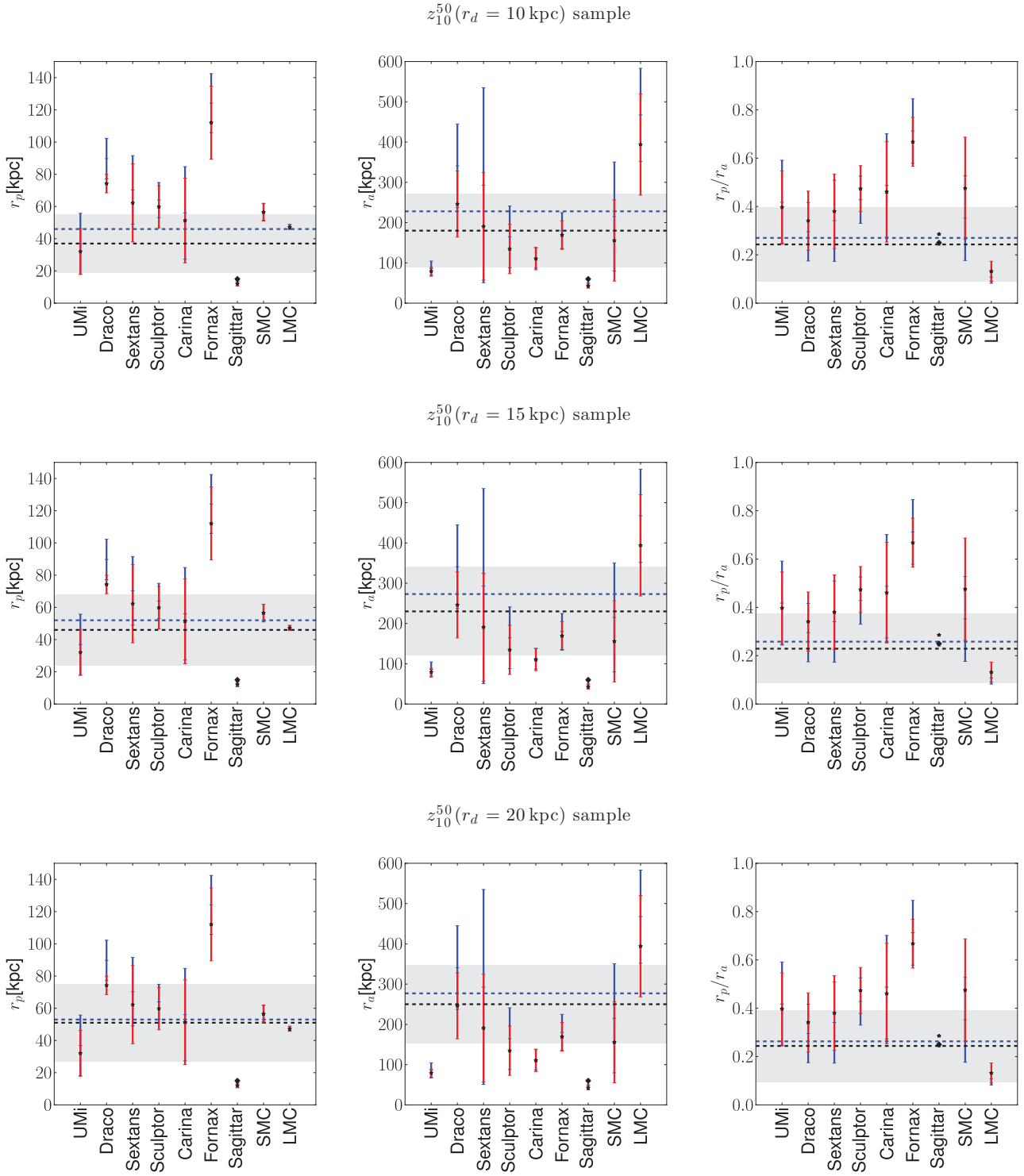

Figure 10. As in Fig. 9, but for three different samples taking disc depletion into account.

have smaller pericentres. This trend is largely driven by UMi and Fornax, and *Gaia* quality data will be required to test it convincingly. (Recall that we do not consider Sagittarius, the SMC and the LMC since these are significantly more massive and therefore less prone to environmental effects.) None the less, our results appear to favour a suppression rather than an enhancement of star formation for dwarfs with small pericentres, consistent with Mayer et al. (2007).

3.4.3 Fossils of reionization

In this section we now compare our derived orbit distribution for the MW dwarfs with the orbits of subhaloes in the VL1 simulation. As discussed in Section 1, there are many more subhaloes in the VL1 simulation than observed dwarfs. We select two interesting subsets: the 50 most massive now (z_0^{50}; top panels of Fig. 9) and the 50 most massive before redshift $z = 10.59$ (z_{10}^{50}; bottom panels

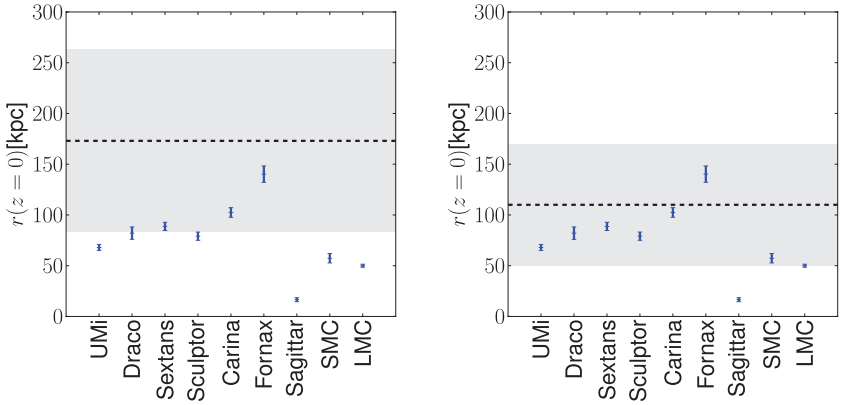

Figure 11. Current radii for nine MW dwarfs with observed proper motions with errors. Overlaid are the mean and standard deviation averaged over the last 2 Gyr of the values from VL1 for the 50 most massive at $z = 0$ (left-hand panel) and for the 50 most massive before $z = 10$ (right-hand panel), respectively (grey band, dashed line).

of Fig. 9). The former explores the idea that the dwarfs' luminosity is monotonically related to their current mass (e.g. Dekel & Silk 1986). The latter explores the idea that the dwarfs form early before reionization (e.g. Efstathiou 1992).

Our derived mean apocentre distances r_a are lower than the mean of the z_0^{50} VL1 subhaloes. This discrepancy cannot be explained by a bias due to the proper motion errors as this effect has the wrong sign (see Section 2.5.6; and note that the blue dashed lines are always above the black dashed lines). Interestingly, however, the mean of our z_{10}^{50} sample (the 50 most massive before redshift $z = 10$) agrees well with the observed mean. This lends further support to the idea that the MW's dwarfs formed early before reionization (e.g. Efstathiou 1992; Barkana & Loeb 1999; Bullock et al. 2000; Benson et al. 2002; Kravtsov et al. 2004; Diemand et al. 2005; Ricotti & Gnedin 2005; Gnedin & Kravtsov 2006; Moore et al. 2006; Maccio' et al. 2010).

Our recovered mean pericentre for all nine dwarfs is higher than the mean of both our z_0^{50} and z_{10}^{50} samples from the VL1 simulation. As a result, the mean recovered r_p/r_a ratio is also higher in the dwarfs than in the simulation samples. We discuss this next.

3.4.4 Disc depletion

Our recovered mean pericentre for all nine dwarfs is higher than the mean of both our z_0^{50} and z_{10}^{50} samples from the VL1 simulation. This could hint at satellite depletion by the Galactic disc as was recently discussed in D'Onghia et al. (2010). However, proper motion errors will also bias our pericentre measurement to be systematically high which creates a similar effect (see Section 2.5.6; and note that the blue dashed lines are in closer accord with the real dwarf data).

We investigate the influence of satellite depletion by a disc using the three subsets of the VL1 subhaloes: $z_{10}^{50}(r_d = 10\,\mathrm{kpc})$, $z_{10}^{50}(r_d = 15\,\mathrm{kpc})$ and $z_{10}^{50}(r_d = 20\,\mathrm{kpc})$ (see Section 2.2). These explore different effective disc sizes r_d. Fig. 10 shows the same plots as Fig. 9 for the disc depleted samples. We find a trend to higher mean pericentres with larger effective disc radii, but also the mean apocentre increases. Excluding Sagittarius, which is in the process of being disrupted and therefore would not be identified as a surviving subhalo in the simulation, the apocentre distributions in $z_{10}^{50}(r_d = 20\,\mathrm{kpc})$ and $z_{10}^{50}(r_d = 15\,\mathrm{kpc})$ are too high in comparison to the current dwarf distribution. This suggests that the total destruction of satellites within $r_d > 15\,\mathrm{kpc}$ is too extreme. With the current data it is not possible to discriminate between the z_{10}^{50} sample without disc depletion and $z_{10}^{50}(r_d = 10\,\mathrm{kpc})$ with a disc with effective depletion radius $r_d = 10\,\mathrm{kpc}$.

Finally, note that our mean recovered r_p/r_a ratio is also higher in the dwarfs than in the simulation samples, meaning that the orbits are more circular. Unlike the pericentre distribution, this cannot be explained by disc depletion effects. This is because both the pericentres and apocentres increase, leading to a near-constant r_p/r_a distribution (see Fig. 10, right-hand panels). Most likely this apparent circularization is the result of proper motion errors biasing our derived pericentres to be high (note that the blue dashed lines are above the black dashed lines in the right-hand panels of Fig. 9). Testing this convincingly will require *Gaia* quality data.

4 CONCLUSIONS

We have evaluated how well we can recover the orbits of MW satellites in the light of measurement errors and model limitations. To do this, we compared orbits in a high-resolution cosmological simulation of a MW analogue with similar orbits integrated in a fixed background potential. We found the following.

(i) With current measurement errors, we can recover the last apocentre r_a and pericentre r_p to ∼40 per cent.

(ii) With *Gaia* quality proper motion data, we can recover r_a and r_p to ∼14 per cent, respectively, and the orbital period t backwards over two orbits. In this regime, we become limited by model systematics rather than measurement error – in particular, how well we can approximate the shape of the MW potential, and how strongly orbits are affected by satellite–satellite interactions in infalling loose groups.

(iii) Recovering full *3D* orbits – the 3D pericentre $\boldsymbol{r}_p$ and apocentre $\boldsymbol{r}_a$ – remains extremely challenging. This is due to a strong dependence on the potential shape that changes over time.

(iv) Comparing only current radial distributions (see Fig. 11) of subsets of satellites in simulations can be misleading. The spatial distribution of subhaloes selected in different ways (e.g. most massive today; most massive before reionization) can be very similar. However, the *orbital distributions* of these subhaloes show stronger discriminatory power.

We applied our orbit-recovery technique to nine MW dwarfs with observed proper motions to determine their last pericentre and apocentre distances r_p and r_a with realistic errors. We found the following.

(i) The mean recovered apocentres are lower than the mean of the most massive simulation subhaloes at redshift $z = 0$, but consistent with the mean of the most massive subhaloes that form before $z = 10$. This lends further support to the idea that dwarfs formed early before reionization.

(ii) To reliably test the effects of satellite depletion by the disc *Gaia* quality data are necessary.

(iii) With the current data a clear relation between SFH and environment cannot be established.

ACKNOWLEDGMENTS

The authors would like to thank J. Guedes for providing her VL1 triaxiality data and the anonymous referee for useful comments that improved the clarity of this paper.

REFERENCES

Aparicio A., Carrera R., Martínez-Delgado D., 2001, AJ, 122, 2524
Barkana R., Loeb A., 1999, ApJ, 523, 54
Bekki K., 2008, ApJ, 684, L87
Bekki K., Chiba M., 2005, MNRAS, 356, 680
Benson A. J., Frenk C. S., Lacey C. G., Baugh C. M., Cole S., 2002, MNRAS, 333, 177
Besla G., Kallivayalil N., Hernquist L., Robertson B., Cox T. J., van der Marel R. P., Alcock C., 2007, ApJ, 668, 949
Besla G., Kallivayalil N., Hernquist L., van der Marel R. P., Cox T. J., Robertson B., Alcock C., 2009, in van Loon J. T., Oliveira J. M., eds, Proc. IAU Symp. 256, The Binarity of the Clouds and the Formation of the Magellanic Stream. Cambridge Univ. Press, Cambridge, p. 99
Blitz L., Robishaw T., 2000, ApJ, 541, 675
Bullock J. S., Kravtsov A. V., Weinberg D. H., 2000, ApJ, 539, 517
Carrera R., Aparicio A., Martínez-Delgado D., Alonso-García J., 2002, AJ, 123, 3199
Chandrasekhar S., 1943, ApJ, 97, 255
Chen J., Kravtsov A. V., Prada F., Sheldon E. S., Klypin A. A., Blanton M. R., Brinkmann J., Thakar A. R., 2006, ApJ, 647, 86
Chou M. et al., 2007, ApJ, 670, 346
Coleman M. G., de Jong J. T. A., 2008, ApJ, 685, 933
Colín P., Avila-Reese V., Valenzuela O., 2000, ApJ, 542, 622
Dekel A., Silk J., 1986, ApJ, 303, 39
Diemand J., Madau P., Moore B., 2005, MNRAS, 364, 367
Diemand J., Kuhlen M., Madau P., 2007a, ApJ, 657, 262
Diemand J., Kuhlen M., Madau P., 2007b, ApJ, 667, 859
Dinescu D. I., Girard T. M., van Altena W. F., López C. E., 2005, ApJ, 618, L25
Dolphin A. E., Weisz D. R., Skillman E. D., Holtzman J. A., 2005, preprint (astro-ph/0506430)
D'Onghia E., Lake G., 2008, ApJ, 686, L61
D'Onghia E., Springel V., Hernquist L., Keres D., 2010, ApJ, 709, 1138
Efstathiou G., 1992, MNRAS, 256, 43P
Evans C. J., Howarth I. D., 2008, MNRAS, 386, 826
Gallart C., Martínez-Delgado D., Gómez-Flechoso M. A., Mateo M., 2001, AJ, 121, 2572
Gnedin N. Y., Kravtsov A. V., 2006, ApJ, 645, 1054
Guedes J., Madau P., Kuhlen M., Diemand J., Zemp M., 2009, ApJ, 702, 890
Harris J., Zaritsky D., 2006, AJ, 131, 2514
Harris J., Zaritsky D., 2009, AJ, 138, 1243
Hashimoto Y., Funato Y., Makino J., 2003, ApJ, 582, 196
Hatzidimitriou D., Croke B. F., Morgan D. H., Cannon R. D., 1997, A&AS, 122, 507
Hernquist L., 1990, ApJ, 356, 359
Ibata R. A., Gilmore G., Irwin M. J., 1994, Nat, 370, 194
Johnston K. V., Law D. R., Majewski S. R., 2005, ApJ, 619, 800
Jones B. F., Klemola A. R., Lin D. N. C., 1989, BAAS, 21, 1107
Kallivayalil N., van der Marel R. P., Alcock C., 2006a, ApJ, 652, 1213
Kallivayalil N., van der Marel R. P., Alcock C., Axelrod T., Cook K. H., Drake A. J., Geha M., 2006b, ApJ, 638, 772
Kim S., Staveley-Smith L., Dopita M. A., Freeman K. C., Sault R. J., Kesteven M. J., McConnell D., 1998, ApJ, 503, 674
Kleyna J. T., Wilkinson M. I., Evans N. W., Gilmore G., 2001, ApJ, 563, L115
Klimentowski J., Lokas E. L., Knebe A., Gottloeber S., Martinez-Vaquero L. A., Yepes G., Hoffman Y., 2010, MNRAS, 402, 1899
Klypin A., Kravtsov A. V., Valenzuela O., Prada F., 1999, ApJ, 522, 82
Koposov S. et al., 2008, ApJ, 686, 279
Koposov S. E., Yoo J., Rix H., Weinberg D. H., Macciò A. V., Escudé J. M., 2009, ApJ, 696, 2179
Kravtsov A. V., Gnedin O. Y., Klypin A. A., 2004, ApJ, 609, 482
Kuhlen M., Diemand J., Madau P., 2007, ApJ, 671, 1135
Kunder A., Chaboyer B., 2009, AJ, 137, 4478
Law D. R., Johnston K. V., Majewski S. R., 2005, ApJ, 619, 807
Lee M. G., Yuk I., Park H. S., Harris J., Zaritsky D., 2009, ApJ, 703, 692
Li Y.-S., Helmi A., 2008, MNRAS, 385, 1365
Maccio' A. V., Kang X., Fontanot F., Somerville R. S., Koposov S. E., Monaco P., 2010, MNRAS, 402, 1995
Majewski S. R., Skrutskie M. F., Weinberg M. D., Ostheimer J. C., 2003, ApJ, 599, 1082
Majewski S. R. et al., 2004, AJ, 128, 245
Mastropietro C., Moore B., Mayer L., Wadsley J., Stadel J., 2005, MNRAS, 363, 509
Mateo M. L., 1998, ARA&A, 36, 435
Mateo M., Olszewski E. W., Walker M. G., 2008, ApJ, 675, 201
Mayer L., Wadsley J., 2004, in Prada F., Martinez Delgado D., Mahoney T. J., eds, ASP Conf. Ser. Vol. 327, Sweeping and Shaking Dwarf Satellites. Astron. Soc. Pac., San Francisco, p. 230
Mayer L., Governato F., Colpi M., Moore B., Quinn T., Wadsley J., Stadel J., Lake G., 2001, ApJ, 559, 754
Mayer L., Kazantzidis S., Mastropietro C., Wadsley J., 2007, Nat, 445, 738
McConnachie A. W., Irwin M. J., 2006, MNRAS, 365, 902
McConnachie A. W. et al., 2008, ApJ, 688, 1009
Miyamoto M., Nagai R., 1975, PASJ, 27, 533
Moore B., Ghigna S., Governato F., Lake G., Quinn T., Stadel J., Tozzi P., 1999, ApJ, 524, L19
Moore B., Diemand J., Madau P., Zemp M., Stadel J., 2006, MNRAS, 368, 563
Navarro J. F., Frenk C. S., White S. D. M., 1996, ApJ, 462, 563
Noël N. E. D., Aparicio A., Gallart C., Hidalgo S. L., Costa E., Méndez R. A., 2009, ApJ, 705, 1260
Perryman M. A. C. et al., 2001, A&A, 369, 339
Piatek S. et al., 2002, AJ, 124, 3198
Piatek S., Pryor C., Olszewski E. W., Harris H. C., Mateo M., Minniti D., Tinney C. G., 2003, AJ, 126, 2346
Piatek S., Pryor C., Olszewski E. W., Harris H. C., Mateo M., Minniti D., Tinney C. G., 2004, AJ, 128, 951
Piatek S., Pryor C., Bristow P., Olszewski E. W., Harris H. C., Mateo M., Minniti D., Tinney C. G., 2005, AJ, 130, 95
Piatek S., Pryor C., Bristow P., Olszewski E. W., Harris H. C., Mateo M., Minniti D., Tinney C. G., 2006, AJ, 131, 1445
Piatek S., Pryor C., Bristow P., Olszewski E. W., Harris H. C., Mateo M., Minniti D., Tinney C. G., 2007, AJ, 133, 818
Press W. H., Teukolsky S. A., Vetterling W. T., Flannery B. P., 1992, Numerical Recipes in C. The Art of Scientific Computing, 2nd edn. Cambridge Univ. Press, Cambridge
Read J. I., Pontzen A. P., Viel M., 2006, MNRAS, 371, 885
Read J. I., Lake G., Agertz O., Debattista V. P., 2008, MNRAS, 389, 1041
Ricotti M., Gnedin N. Y., 2005, ApJ, 629, 259
Sales L. V., Navarro J. F., Abadi M. G., Steinmetz M., 2007, MNRAS, 379, 1475
Scholz R.-D., Irwin M. J., 1994, in MacGillivray H. T., ed., Proc. IAU Symp. 161, Absolute Proper Motions of the Dwarf Spheroidal Galaxies in Draco and Ursa Minor. Kluwer, Dordrecht, p. 535

Siegel M. H. et al., 2007, ApJ, 667, L57
Simon J. D., Geha M., 2007, ApJ, 670, 313
Stanimirović S., Staveley-Smith L., Jones P. A., 2004, ApJ, 604, 176
Strigari L. E., Bullock J. S., Kaplinghat M., Diemand J., Kuhlen M., Madau P., 2007, ApJ, 669, 676
van den Bergh S., 1994, AJ, 107, 1328
van der Marel R. P., Alves D. R., Hardy E., Suntzeff N. B., 2002, AJ, 124, 2639
Walker M. G., Mateo M., Olszewski E. W., 2008, ApJ, 688, L75
Wilkinson M. I., Evans N. W., 1999, MNRAS, 310, 645
Zemp M., Stadel J., Moore B., Carollo C. M., 2007, MNRAS, 376, 273
Zentner A. R., Bullock J. S., 2003, ApJ, 598, 49
Zhao H., 2004, MNRAS, 351, 891

This paper has been typeset from a TEX/LATEX file prepared by the author.